Design of experiment for model discrimination: SFE case, part II

Oliwer Sliczniuk[a,*]

[a]*Aalto University, School of Chemical Engineering, Espoo, 02150, Finland*

ARTICLE INFO

ABSTRACT

This study investigates the process of chamomile oil extraction from flowers. A parameter-distributed model consisting of a set of partial differential equations is used to describe the governing mass transfer phenomena in a solid-fluid environment under supercritical conditions using carbon dioxide as a solvent. The concept of quasi-one-dimensional flow is applied to reduce the number of spatial dimensions. The flow is assumed to be uniform across any cross-section, although the area available for the fluid phase can vary along the extractor. The physical properties of the solvent are estimated from the Peng-Robinson equation of state. Based on the set of laboratory experiments performed under multiple constant operating conditions: $30 - 40°C$, $100 - 200$ bar, and $3.33 - 6.67 \cdot 10^{-5}$ kg/s, two process models are developed: a first-principle and a data-driven model. The goal of this work is to design a dynamic experiment to discriminate between two competing process models.

1. Introduction

Supercritical CO_2 is defined as carbon dioxide that is pressurized and heated above its critical point (31.1 °C, 74 bar). Depending on the operating conditions, the fluid properties such as viscosity and density can vary, which leads to multiple industrial applications of CO_2.

One of the most popular applications of supercritical CO_2 is the extraction of essential oils, as described by many researchers, for example, by Sodeifian and Sajadian [1], Reverchon et al. [2] or Sovova [3]. Traditional methods, such as distillation and organic solvent extraction, are commonly employed but have drawbacks. Distillation, involves high temperatures that can lead to the thermal degradation of heat-sensitive compounds. This limitation has increased the popularity of alternative techniques, such as supercritical fluid extraction. Supercritical CO_2 is appealing due to its distinctive properties: it is inflammable, non-toxic and non-corrosive. Supercritical fluids can exhibit both gas- and liquid-like properties, allowing for adjustable dissolving power through changes in operating conditions.

The applications of supercritical carbon dioxide are not limited only to an extraction process but can also be used for impregnation as described by Weidner [4], Machado et al. [5] or Fathi et al. [6]. Impregnation is defined as modifying the properties of bulk substances by physically or chemically binding/adsorbing impregnates to a bulk material or surface, such as the hydrophobization of surfaces. The main advantage of using supercritical CO_2 is that after depressurization, it desorbs from the surface and evaporates, leaving a solvent-free product. On the other hand, the main disadvantage of using carbon dioxide for impregnation is the low solubility of many drugs of interest.

Another application of supercritical CO_2 is nanoparticles formation as investigated by Padrela et al. [7], Franco and De Marco [8], Saadati Ardestani et al. [9] or Sodeifian

et al. [10]. Supercritical carbon-dioxide-assisted technologies enable the production of different morphologies of different sizes, including nanoparticles and nanocrystals, by modulating operating conditions. Supercritical fluid-based processes have advantages over techniques conventionally employed to produce nanosized particles or crystals, such as reduced use of toxic solvents. Moreover, the CO_2 is completely removed from the final product by simple depressurization.

This study investigates the extraction of essential oil from chamomile flowers (Matricaria chamomilla L.) via supercritical fluid extraction techniques and the modelling of this process. Chamomile is a medicinal herb widely cultivated in southern and eastern Europe — in countries such as Germany, Hungary, France and Russia. It can be found outside Europe, for instance in Brazil as discussed by Singh et al. [11]. This plant is distinguished by its hollow, bright gold cones, housing disc or tubular florets and surrounded by about fifteen white ray or ligulate florets. Chamomile has been used for its medicinal benefits, serving as an anti-inflammatory, antioxidant, mild astringent, and healing remedy. Extracts of chamomile are widely used to calm nerves and mitigate anxiety, hysteria, nightmares, insomnia and other sleep-related conditions, according to Srivastava [12]. Orav et al. [13] reported that oil yields from dried chamomile samples ranged from 0.7 to 6.7 mL/kg. The highest yields of essential oil, between 6.1 and 6.7 mL/kg, were derived from chamomile sourced from Latvia and Ukraine. In comparison, chamomile from Armenia exhibited a lower oil content of 0.7 mL/kg.

The literature offers various mathematical models to describe the extraction of valuable compounds from biomass. Selecting a process model is case-to-case dependent and requires analysis of each model's specific assumptions about mass transfer and thermodynamic equilibrium.

Goto et al. [14] presented the Shrinking Core (SC) model, which describes a process of irreversible desorption that is followed by diffusion through the pores of a porous solid. When the mass transfer rate of the solute in the non-extracted inner region is significantly slower than in the outer

*Corresponding author
✉ oliwer.sliczniuk@aalto.fi (O. Sliczniuk)
ORCID(s): 0000-0003-2593-5956 (O. Sliczniuk); 0000-0002-0183-5558 (P. Oinas)

region, where most of the solute has already been extracted, or when the solute concentration exceeds its solubility in the solvent, a distinct boundary may form between the inner and outer regions. As extraction progresses, the core of the inner region shrinks. The model envisions supercritical CO_2 extraction as a sharp, inward-moving front, with a completely non-extracted core ahead of the front and a fully extracted shell behind it.

Sovova [3] proposed The Broken-and-Intact Cell (BIC) model, which assumes that a portion of the solute, initially stored within plant structures and protected by cell walls, is released during the mechanical breakdown of the material. The solute located in the region of broken cells near the particle surface is directly exposed to the solvent, while the core of the particle contains intact cells with undamaged walls. This model describes three extraction phases: a fast extraction phase for accessible oil, a transient phase, and a slow phase controlled by diffusion. The model has been successfully applied to the extraction of grape oil (Sovová et al. [15]) and caraway oil (Sovova et al. [16]).

The Supercritical Fluid Extraction (SFE) process can be be treated similarly to heat transfer, considering solid particles like hot balls cooling down in a uniform environment. Bartle et al. [17] introduced the hot ball diffusion (HBD) model, where spherical particles with uniformly distributed solute diffuse similarly to heat diffusion. Unlike the BIC model, where solute is readily available on the particle surface, the HBD model is suited for systems with small quantities of extractable materials and is not limited by solubility. The model is particularly relevant when internal diffusion controls mass transfer, allowing results from single particles to be extended to the entire bed under uniform conditions. Reverchon et al. [2] have further elaborated on the HBD model and used it to simulate extraction processes for natural materials.

Reverchon [18] proposed a model for extraction of essential oils, which are mainly located inside the vegetable cells in organules called vacuoles. Only a small fraction of essential oil might be near the particle surface due to the breaking up of cells during grinding or in epidermal hairs located on the leaf surface. The fraction of oil freely available on the particle surface should not be significant in the case of SFE from leaves. Consequently, SFE of essential oil from leaves should be mainly controlled by the internal mass-transfer resistance. Therefore, the external mass-transfer coefficient was neglected in the development of the model of Reverchon [18]. The mass balances were developed in the additional hypotheses that the axial dispersion can be neglected and that the solvent density and flow rate are constant along the bed.

This work builds upon the linear kinetic model suggested by Reverchon [18], deriving fundamental governing equations to develop a comprehensive model for the chamomile oil extraction process. This model aims for control-oriented simplicity, assuming a semi-continuous operation within a cylindrical vessel. The process involves a supercritical solvent being pumped through a fixed bed

of finely chopped biomass to extract the solute, followed by separation of the solvent and solute in a flush drum to collect the extract. Parameters such as pressure (P), feed flow rate (F) and inlet temperature (T_{in}) are adjustable and measurable, while the outlet temperature (T_{out}) and the amount of product at the outlet can only be monitored. Figure 1 presents a simplified process flow diagram.
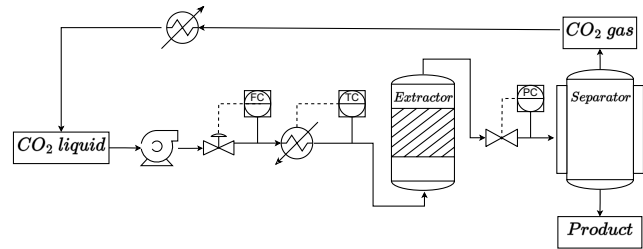

Figure 1: Process flow diagram.

In the study of dynamical systems, selecting the most accurate model to represent a physical process is crucial for effective prediction, control, and understanding of underlying mechanisms. When multiple models are trained on the same dataset but exhibit subtle structural differences, their responses may diverge in nuanced ways. Traditional model selection criteria often fail to capture these subtleties, making it necessary to employ a robust statistical framework for optimal model discrimination.

The process of discriminating between competing models typically follows a sequential approach, involving two iterative steps. The first is the design phase, where a discrimination criterion is used to select the next experiment. This criterion, which reflects the information content of potential experimental conditions, helps identify the experiment that is expected to provide the most information for distinguishing between models. Once the experiment is conducted, the second step—data analysis—is performed. A stopping rule is then applied to determine if one model can be deemed significantly better than the others. If no clear distinction is made, the process is repeated. Most model discrimination criteria rely on either maximum divergence or maximum entropy principles.

Building on information theory and a Bayesian approach, Box and Hill [19] introduced a sequential design procedure for model discrimination. Since entropy measures the amount of available information about a system, additional experiments should be selected to maximize the expected change in entropy, thereby increasing the information obtained about the system through successive experiments.

Buzzi-Ferraris and Forzatti [20] observed that the performance of Box's sequential design for model discrimination depends on the order in which experimental observations are processed. This is due to the recursive nature of updating model probabilities. As model probabilities should be independent of the data presentation order, the authors noted that experiments should be selected in regions where differences in prediction variances are large, rather than where differences in model responses are most pronounced.

They applied this approach to two cases: ammonia synthesis from nitrogen and hydrogen, and vapor-phase chlorination of tetrachloroethane using activated silica gel at 200 °C.

Chen and Asprey [21] proposed a novel method for designing optimally informative dynamic experiments aimed at discriminating among several competing multiresponse nonlinear dynamic models, which are generally described by systems of differential and algebraic equations. Their approach extends Buzzi-Ferraris and Forzatti [20]' discrimination criterion to dynamic systems, reformulating the experimental design problem as an optimal control problem. This method was applied to the fed-batch fermentation of Baker's yeast, with the goal of discriminating between four competing models by identifying optimal profiles for the dilution factor and inlet substrate concentration.

2. Materials and methods

2.1. Governing equations

Following the work of Anderson [22], the governing equations for a quasi-one-dimensional flow were derived. A quasi-one-dimensional flow refers to a fluid flow scenario assuming that the flow properties are uniformly distributed across any cross-section. This simplification is typically applied when the flow channel's cross-sectional area changes, such as through irregular shapes or partial filling of an extractor. According to this assumption, velocity and other flow properties change solely in the flow direction.

As discussed by Anderson [23], all flows are compressible, but some of them can be treated as incompressible since the velocities are low. This assumption leads to the incompressible condition: $\nabla \cdot u = 0$, which is valid for constant density (strict incompressible) or varying density flow. The assumption allows for removing acoustic waves and large perturbations in density and/or temperature. In the 1-D case, the incompressibility condition becomes $\frac{du}{dz} = 0$, so the fluid velocity is constant along the $z-$ direction.

The set of quasi-one-dimensional governing equations in Cartesian coordinates is described by Equations 1 - 3:

$$\frac{\partial \left(\rho_f A_f \right)}{\partial t} + \frac{\partial \left(\rho_f A_f v \right)}{\partial z} = 0 \tag{1}$$

$$\frac{\partial \left(\rho_f v A_f \right)}{\partial t} + \frac{\partial \left(\rho_f A_f v^2 \right)}{\partial z} = -A_f \frac{\partial P}{\partial z} \tag{2}$$

$$\frac{\partial \left(\rho_f e A_f \right)}{\partial t} + \frac{\partial \left(\rho_f A_f v e \right)}{\partial z} = -P \frac{\left(A_f v \right)}{\partial z} + \frac{\partial}{\partial z} \left(k \frac{\partial T}{\partial z} \right) \tag{3}$$

where ρ_f is the density of the fluid, A_f is the function which describes a change in the cross-section, v is the velocity, P is the total pressure, e is the internal energy of the fluid, t is time and z is the spatial direction.

2.2. Extraction model
2.2.1. Continuity equation

The previously derived quasi-one-dimensional continuity equation (Equation 1) is redefined by incorporating the function $A_f = A\phi$. This modification distinguishes constant and varying terms, where the varying term accounts for changes in the cross-sectional area available for the fluid. Equation 4 shows the modified continuity equation:

$$\frac{\partial(\rho_f \phi)}{\partial t} + \frac{\partial(\rho_f v A \phi)}{\partial z} = 0 \tag{4}$$

where A is the total cross-section of the extractor and ϕ describes porosity along the extractor.

Assuming that the mass flow rate is constant in time, the temporal derivative becomes the mass flux F, and the spatial derivative can be integrated along z as

$$\int \frac{\partial(\rho_f v A \phi)}{\partial z} dz = F \rightarrow F = \rho_f v A \phi \tag{5}$$

To simplify the system dynamics, it is assumed that F is a control variable and affects the whole system instantaneously (due to $\nabla \cdot u = 0$), which allows finding the velocity profile that satisfies mass continuity based on F, ϕ and ρ_f:

$$v = \frac{F}{\rho_f A \phi} \tag{6}$$

Similarly, superficial velocity may be introduced:

$$u = v\phi = \frac{F}{\rho_f A} \tag{7}$$

The fluid density ρ_f can be obtained from the Peng-Robinson equation of state if the temperature and thermodynamic pressure are known along z. Variation in fluid density may occur due to pressure or inlet temperature changes. In a non-isothermal case, in Equations 6 and 7 ρ_f is considered the average fluid density along the extraction column.

2.2.2. Mass balance for the fluid phase

Equation 8 describes the movement of the solute in the system, which is constrained to the axial direction due to the quasi-one-dimensional assumption. Given that the solute concentration in the solvent is negligible, the fluid phase is described as pseudo-homogeneous, with properties identical to those of the solvent itself. It is also assumed that the thermodynamic pressure remains constant throughout the device. The analysis further simplifies the flow dynamics by disregarding the boundary layer near the extractor's inner wall. This leads to a uniform velocity profile across any cross-section perpendicular to the axial direction. Thus, the mass balance equation includes convection, diffusion and kinetic terms representing the fluid phase behaviour:

$$\frac{\partial c_f}{\partial t} + \frac{1}{\phi} \frac{\partial \left(c_f u \right)}{\partial z} = \frac{1 - \phi}{\phi} r_e + \frac{1}{\phi} \frac{\partial}{\partial z} \left(D_e^M \frac{\partial c_f}{\partial z} \right) \tag{8}$$

where c_f represents the solute concentration in the fluid phase, r_e is the mass transfer kinetic term and D_e^M is the axial diffusion coefficient.

2.2.3. Mass balance for the solid phase

As given by Equation 9, the solid phase is considered stationary, without convection and diffusion terms in the mass balance equation. Therefore, the only significant term in this equation is the kinetic term of Equation 10, which connects the solid and fluid phases. For simplicity, the extract is represented by a single pseudo-component:

$$\frac{\partial c_s}{\partial t} = \underbrace{r_e}_{\text{Kinetics}} \tag{9}$$

2.2.4. Kinetic term

As the solvent flows through the fixed bed, CO_2 molecules diffuse into the pores, adsorb on the inner surface and form a film due to solvent-solid matrix interactions. The dissolved solute diffuses from the particle's core through the solid-fluid interface, the pore and the film into the bulk. Figure 2 shows the mass transfer mechanism, where the mean solute concentration in the solid phase is denoted as c_s, and the equilibrium concentrations at the solid-fluid interface are denoted as c_s^* and c_p^* for the solid and fluid phases, respectively. The concentration of the solutes in the fluid phase in the centre of the pore is denoted as c_p. As the solute diffuses through the pore, its concentration changes, reaching c_{pf} at the opening. Then, the solute diffuses through the film around the particle and reaches bulk concentration c_f. The two-film theory describes the solid-fluid interface inside the pore. The overall mass transfer coefficient can be determined from the relationship between the solute concentration in one phase and its equilibrium concentration.
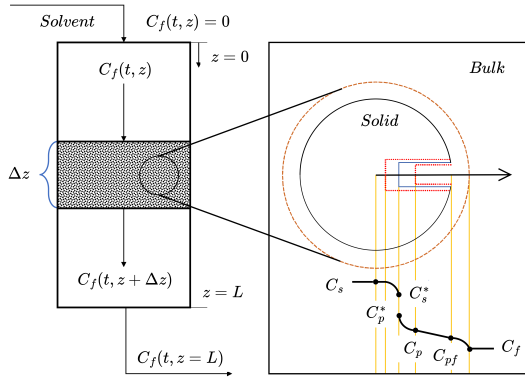

Figure 2: Mass transfer mechanism.

Bulley et al. [24] suggest a process where the driving force for extraction is given by the difference between the concentration of the solute in the bulk, c_f, and in the centre of the pore, c_p^*. The concentration c_p^* is in equilibrium with c_s according to the equilibrium relationship. The rate of extraction is thus $r_e \left(c_f - c_p^*(c_s) \right)$. In contrast, Reverchon [18] proposes a driving force given by the difference between c_s and c_p^*. As given by Equation 10, the concentration c_p^* is determined by the equilibrium relationship with c_f:

$$r_e = \frac{D_i}{\mu l^2} \left(c_s - c_p^* \right) \tag{10}$$

where μ is sphericity, l a characteristic dimension of particles that can be defined as $l = r/3$, r is the mean particle radius, ρ_s is the solid density, D_i corresponds to the overall diffusion coefficient and c_P^* is the concentration at the solid-fluid interface (which according to the internal resistance model is supposed to be at equilibrium with the fluid phase).

According to Bulley et al. [24], a linear equilibrium relationship (Equation 11) can be used to find the equilibrium concentration of the solute in the fluid phase c_f^* based on the concentration of the solute in the solid phase c_s:

$$c_f^* = k_p c_s \tag{11}$$

The volumetric partition coefficient k_p acts as an equilibrium constant between the solute concentration in one phase and the corresponding equilibrium concentration at the solid-fluid interphase. Spiro and Kandiah [25] proposed to define the mass partition coefficient k_m as

$$k_m = \frac{k_p \rho_s}{\rho_f} \tag{12}$$

According to Reverchon [18], the kinetic term becomes

$$r_e = -\frac{D_i}{\mu l^2} \left(c_s - \frac{\rho_s c_f}{k_m \rho_f} \right) \tag{13}$$

2.2.5. Uneven solute's distribution in the solid phase

Following the idea of the Broken-and-Intact Cell (BIC) model (Sovova [26]), the internal diffusion coefficient D_i is considered to be a product of the reference value of D_i^R and the exponential decay function γ, as given by Equation 14:

$$D_i = D_i^R \gamma(c_s) = D_i^R \exp\left(\Upsilon \left(1 - \frac{c_s}{c_{s0}} \right) \right) \tag{14}$$

where Υ describes the curvature of the decay function. Equation 15 describes the final form of the kinetic term:

$$r_e = -\frac{D_i^R \gamma}{\mu l^2} \left(c_s - \frac{\rho_s c_f}{k_m \rho_f} \right) \tag{15}$$

The γ function limits the solute's availability in the solid phase. Similarly to the BIC model, the solute is assumed to be contained in the cells, some of which are open because the cell walls were broken by grinding, with the rest remaining intact. The diffusion of the solute from a particle's core takes more time than the diffusion of the solute close to the outer surface. The same idea can be represented by the decaying internal diffusion coefficient, where the decreasing term is a function of the solute concentration in the solid.

An alternative interpretation of the decay function γ involves considering the porous structure of the solid particles, where the pores are initially saturated with the solute. During extraction, the solute within these pores gradually dissolves into the surrounding fluid. Initially, the solute molecules near the pore openings dissolve and diffuse rapidly due to the short diffusion paths. As the extraction progresses, the dissolution front moves deeper into the pore structure, and solute from the inner regions of the pores begins to dissolve. The diffusion of solute molecules from the interior of the pores to the external fluid becomes progressively slower because the effective diffusion path length increases. This lengthening of the diffusion path enhances the mass transfer resistance, reducing the overall diffusion rate.

In an extreme case, this model could be compared with the Shrinking Core Model presented by Goto et al. [14], where the particle radius decreases as the solute content in the solid phase diminishes. In the SC model, the reduction in particle size leads to significant changes in both the diffusion path length and the surface area available for mass transfer. The diminishing particle size increases the diffusion path within the remaining solid core and decreases the external

surface area, both of which contribute to a slower extraction rate. By comparing this to the varying diffusion coefficient in our model, some conceptual similarities can be noticed.

2.2.6. Empirical correlations

The empirical correlations for D_i and Υ were derived by Sliczniuk and Oinas [27] and validated for temperatures between $30 - 40\,°C$, pressures between $100 - 200$ bar, and mass flow rates between $3.33 - 6.67 \cdot 10^{-5}$ kg/s. Figures 3 and 4 show the results of multiple linear regression applied to solutions of parameter estimation and selected independent variables. The region marked with the white dashed line represents the confidence region, where the model has been tested. Both correlations should be equal of greater than zero, to avoid unphysical behaviour such as the reverse mass transfer. The multiple linear regression functions are combined with the rectifier function to ensure the non-negativity.
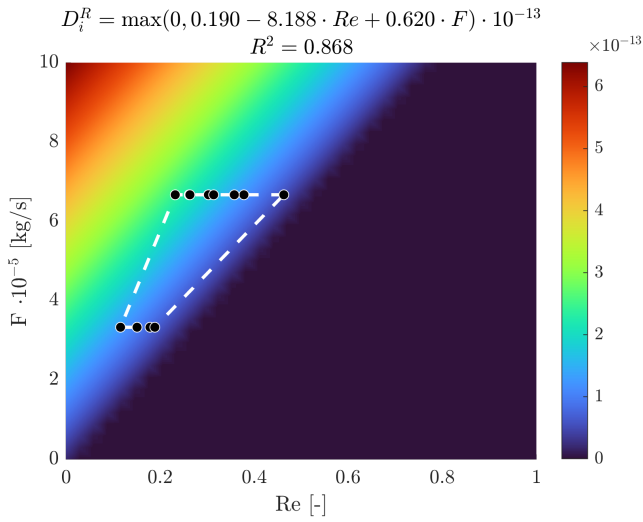

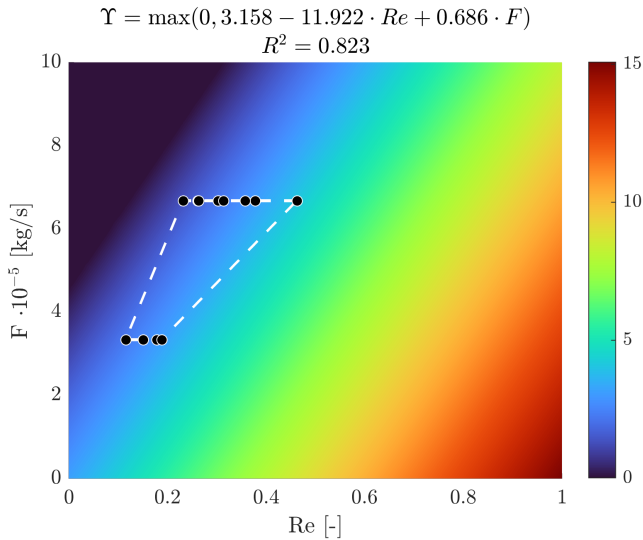Figure 3: Multiple linear regression $D_i^R = f(Re, F)$

Figure 4: Multiple linear regression $\Upsilon = f(Re, F)$

2.2.7. Heat balance

The heat balance equation describe the evolution of the enthalpy in the system and it is given by Equation 16

$$\frac{\partial \left(\rho_f h A_f \right)}{\partial t} = -\frac{\partial \left(\rho_f h A_f v \right)}{\partial z} + \frac{\partial \left(P A_f \right)}{\partial t} + \frac{\partial}{\partial z}\left(k \frac{\partial T}{\partial z} \right) \tag{16}$$

If the value of enthalpy h is known from the time evolution of the energy equation, and pressure P is known from measurement, then the temperature T can be reconstructed based on the departure function. The departure function is a mathematical function that characterizes the deviation of a thermodynamic property (enthalpy, entropy, and internal energy) of a real substance from that of an ideal gas at the same temperature and pressure. As presented by Gmehling et al. [28], for the Peng-Robinson equation of state, the enthalpy departure function is defined by Equation 17.

$$h - h^{id} = RT \left[T_r(Z-1) - 2.078(1+\kappa)\sqrt{\alpha(T)} \ln\left(\frac{Z + \left(1+\sqrt{2}\right)B}{Z + \left(1-\sqrt{2}\right)B} \right) \right] \tag{17}$$

where α is defined as $\left(1 + \kappa \left(1 - \sqrt{T_r}\right)\right)^2$, T_r is the reduced temperature, P_r is the reduced pressure, Z is the compressibility factor, κ is a quadratic function of the acentric factor and B is calculated as $0.07780\frac{P_r}{T_r}$.

Equation 17 requires an reference sate, which is assumed to be $T_{ref} = 298.15$ K and $P_{ref} = 1.01325$ bar.

A root-finder can be used to find a value of temperature, which minimizes the difference between the value of enthalpy coming from the heat balance and the departure functions. The root fining procedure to repeated at every time step to find a temperature profile along spatial direction z.

$$\min_T \left(\underbrace{h(t,x)}_{\text{Heat balance}} - \underbrace{h\left(T, P, \rho_f\left(T, P\right)\right)}_{\text{Departure function}} \right)^2 \tag{18}$$

2.2.8. Pressure term

As explained in Chapters 2.1, this low velocity region, pressure is, nearly constant due to the small pressure wave propagation that occurs at the speed of sound. Under such conditions, the term $\partial P/\partial t$ can be approximated by a difference equation, describing the pressure change in the whole system. The pressure P in the system is considered a state variable, while the pressure in the new time-step P_{in} is considered a control variable.

$$\frac{\partial P}{\partial t} \approx \frac{P_{in} - P}{\Delta t} \tag{19}$$

Such a simplified equation allows for instantaneous pressure change in the system but does not consider a gradual pressure build-up and the effects of pressure losses. In a real system, the dynamics of pressure change would depend on a pump and a back-pressure regulator.

2.2.9. Extraction yield

The process yield is calculated according to Equation 20 as presented by Sovova et al. [16]. The measurement

equation evaluates the solute's mass at the extraction unit outlet and sums it up. The integral form of the measurement (Equation 20) can be transformed into the differential form (Equation 21) and augmented with the process model.

$$y = \int_{t_0}^{t_f} \left. \frac{F}{\rho_f} c_f \right|_{z=L} dt \qquad (20)$$

$$\frac{dy}{dt} = \left. \frac{F}{\rho_f} c_f \right|_{z=L} \qquad (21)$$

2.2.10. Initial and boundary conditions

It is assumed that the solvent is free of solute at the beginning of the process $c_{f0} = 0$, that all the solid particles have the same initial solute content c_{s0}, and that the system is isothermal, hence the initial state is h_0. The fluid at the inlet is considered not to contain any solute. The initial and boundary conditions are defined as follows:

$$c_f(t = 0, z) = 0 \qquad c_s(t = 0, z) = c_{s0} \qquad h(t = 0, z) = h_0$$

$$c_f(t, z = 0) = 0 \qquad h(t, z = 0) = h_{in} \qquad \frac{\partial c_f(t, z = L)}{\partial x} = 0$$

$$\frac{\partial h(t, z = L)}{\partial x} = 0 \qquad c_s(t, z = \{0, L\}) = 0 \qquad y(0) = 0 \quad P(0) = P_0$$

2.2.11. Discretization methods

The method of lines is used to transform the process model equations into a set of ODEs denoted as $G(x; \Theta)$. The backward finite difference is used to approximate the first-order derivative, while the central difference scheme approximates the second-order derivative z direction. The length of the fixed bed is divided into N_z, i.e. equally distributed points in the z direction. The state-space model after discretization is denoted as x and defined as follows:

$$\dot{x} = \frac{dx}{dt} = \begin{bmatrix} \frac{dc_{f,1}}{dt} \\ \vdots \\ \frac{dc_{f,N_z}}{dt} \\ \hline \frac{dc_{s,1}}{dt} \\ \vdots \\ \frac{dc_{s,N_z}}{dt} \\ \hline \frac{dh_1}{dt} \\ \vdots \\ \frac{dh_{N_z}}{dt} \\ \hline \frac{dP}{dt} \\ \hline \frac{dy}{dt} \end{bmatrix} = \underbrace{\begin{bmatrix} G_1(c_f, c_s, h; \Theta) \\ \vdots \\ G_{N_z}(c_f, c_s, h; \Theta) \\ \hline G_{N_z+1}(c_f, c_s, h; \Theta) \\ \vdots \\ G_{2N_z}(c_f, c_s, h; \Theta) \\ \hline G_{2N_z+1}(c_f, c_s, h; \Theta) \\ \vdots \\ G_{3N_z}(c_f, c_s, h; \Theta) \\ \hline G_{3N_z+1}(c_f, c_s, h; \Theta) \\ \hline G_{3N_z+2}(c_f, c_s, h; \Theta) \end{bmatrix}}_{G(x; \Theta)}$$

where $x \in \mathbb{R}^{N_x = 3N_z + 2}$ and $\Theta \in \mathbb{R}^{N_\Theta = N_\theta + N_u}$, N_θ is the number of parameters, N_u is the number of control variables.

For a derivative to be conservative, it must form a telescoping series. In other words, only the boundary terms should remain after adding all terms coming from the discretization over a grid, and the artificial interior points should be cancelled out. Discretization is applied to the conservative form of the model to ensure mass conservation.

3. General function approximators

3.1. Radial Basis Function

An alternative approach to the first principle modelling of physical process is to apply general function approximators and train them based on a dataset. Such an approach has an advantage of not pre-assuming a structure of a model, which results in higher flexibility of a model. On the other hand, this come with a cost of higher number of parameters to be fitted and choosing appropriate function approximator. In this work, a Radial Basis Function (RBF) is used to define $\frac{dc_s}{dt}$ based on a dataset. RBF is a sum real-valued functions (so called kernels) δ whose value depends only on the distance between the input and some fixed point, called a center c, so that $\delta(x) = \delta(||x - c||)$. The distance is usually Euclidean distance, although other metrics are sometimes used. Sums of radial basis functions are typically used to approximate given functions $y(x) = \sum_{i=1}^{N} w_i \delta(||x - c_i||) + b$. Where N corresponds to the number of kernels, w to weight in the summation and b is a bias. The kernel can be defined as a Gaussian, Inverse quadratic, Inverse multiquadratic, Polyharmonic spline etc. In this work, the three-dimensional Gaussian is used. All the kernels are assumed to have the same shape, which means the all have the same widths in the same direction. Following observation from Sliczniuk and Oinas [27], the two independent variables are normalized concentration of the solute in the solid phase, defined as $\tilde{c}_s(t) = 1 - \left(\frac{c_s(t)}{c_{s0}} \right)$, normalized fluid density $\tilde{\rho}_f = \frac{\rho_f}{800}$ and the Reynolds number. The value of the normalizing factor was selected to be the density of CO_2 in the middle of validated range for temperature and pressure. By introducing $\tilde{\rho}_f$ to the extraction kinetic equation, the information on the operating conditions is passed directly to the RBF network. In a sense, $\tilde{\rho}_f$ can be related to the solubility effect, because many empirical solubility correlations depends on fluid density as discussed by Antonie and Pereira [29]. By incorporation the Reynolds number, the hydrodynamic conditions are considered.

$$\begin{aligned} \frac{dc_s}{dt} &= \sum_{i=1}^{N} w_i \delta(||x - c_i||) + b \\ &= \left(\sum_{i=1}^{N} w_i \exp\left(-\frac{(\tilde{c}_s(t) - \tilde{c}_{si}^c)^2}{2\sigma_{\tilde{c}}^2} - \frac{(Re(t) - Re_i^c)^2}{2\sigma_{Re}^2} - \frac{(\tilde{\rho}_f(t) - \tilde{\rho}_{fi}^c)^2}{2\sigma_{\tilde{\rho}_f}^2} \right) + b \right) \cdot 10^{-3} \end{aligned}$$

(22)

where $\tilde{c}_{si}^c$, ρ_f^c and Re_i^c correspond to centres of each Gaussian kernels as defined above. $\sigma_{\tilde{c}}$, σ_{Re} and $\sigma_{\tilde{\rho}_f}$ corresponds to the width of each kernel in direction of $\tilde{c}_{si}$, Re_i and $\tilde{\rho}_f$, respectively. The unknowns of this equation are N,

i	1	2	3	4	5
$\tilde{c}_{si}^c$	-1.5928	-0.3309	-0.5295	-0.4325	1.0018
Re_i^c	0.8784	0.7651	0.3134	0.5102	-0.0815
$\tilde{\rho}_{fi}^c$	-0.3486	-1.0499	-0.0132	1.0903	0.3839
w_i	-1.0250	-2.3195	9.1491	4.0846	1.3380
$\sigma_{\tilde{c}}^2$	1.0423	1.3864	0.4742	0.5479	0.8383
σ_{Re}^2	1.3492	1.9967	0.0361	2.7306	1.8687
$\sigma_{\tilde{\rho}_f}^2$	0.9200	0.3673	1.3347	0.0093	2.0301
b	-1.0812				

Table 1
Parameters of the RBF network

w_i, $\tilde{c}_{si}^c$, Re_i^c and $\tilde{\rho}_{fi}^c$. If N is pre-selected, then the total number of unknowns can calculated as $7N + 1$. The new process model is defined by substituting Equation 9 with 22. The parameter estimation procedure follows Sliczniuk and Oinas [27], with an additional constraint on the positivity of the kinetic term. The obtained parameters are presented in Table 1. Figure 5 shows comparison of kinetic term values determined by the first principle model and the RBF-based model.

Good agreement between the simulation results and the dataset can be observed in Figure 6. The figure compares the yield curves for the first principle (dashed line) and the RBF-based model (dotted line). The calculated mean square error and standard deviation as presented in Table 2.

4. Optimal design of experiment for model discrimination

Multiple alternative models are often proposed to describe the same physical situation. To discriminate between these models, a set of new experiments needs to be performed. Each model attempts to predict the model response y as a function of the experimental conditions Ξ and the model parameters θ (here, θ refers to the model parameters that describe the extraction kinetics and is a subset of the parameter space Θ). What varies from model to model is the mathematical form of the function and the set of parameters involved, although some of the parameters appearing in different models may possess the same physical interpretation.

Following the work of Box and Hill [19], Himmelblau [30] and Bard [31] the ratio of two probability distributions can be used to indicate the measure of evidence in favor of one model over another. Consequently, $\ln\left(\frac{p_1(y)}{p_2(y)}\right)$ becomes a measure of the odds in favor of choosing hypothesis H_1 (i.e., that $p_1(y)$ is the true model) over hypothesis H_2 (i.e., that $p_2(y)$ is the true model). Alternatively, the ratio can be interpreted as the information in favor of hypothesis H_1 as opposed to hypothesis H_2. The so-called "weight of evidence" or expected information in favor of choosing H_1 over H_2 can be defined through the Kullback–Leibler divergence and is represented by:

$$D_{KL}\left(p_1(y)|p_2(y)\right) = \int_{-\infty}^{\infty} p_1(y)\ln\left(\frac{p_1(y)}{p_2(y)}\right) dy \qquad (23)$$

In essence, $D_{KL}(p_1(y)|p_2(y))$ measures how sharply data drawn from p_1 would differ from data drawn from p_2. If $D_{KL}(p_1(y)|p_2(y))$ is large, then it is relatively unlikely that observations coming from p_1 would be mistaken for those coming from p_2. Conversely, $D_{KL}(p_2(y)|p_1(y))$ quantifies how "hard" it would be to confuse data from p_2 with those fro, p_1. One can view these divergences as asymmetric measures of the distance between two probability distributions. If model 1 is correct, then it is desirable to conduct an experiment Ξ that is likely to confirm this, i.e., is expected to produce a larger value of $D_{KL}\left(p_1(y)|p_2(y)\right)$. Conversely, if model 2 is correct, then the experiment Ξ results in a larger value of $D_{KL}\left(p_2(y)|p_1(y)\right)$. Both models assume normal error distributions with predicted covariance matrices Σ_1 and Σ_2, respectively:

$$p_i(y) = \frac{1}{\sqrt{(2\pi)^{n_Y}|\Sigma_i|}}\exp\left(-\frac{1}{2}(Y-y_i)^{\top}\Sigma_i^{-1}(Y-y_i)\right) \qquad (24)$$

where Y is the observed data, y_i is the predicted response from model i, and n_Y is the number of measurements.

In advance of performing the experiment Ξ, the output Y is unknown, so D_{KL} cannot be computed directly. However, its expected value under the assumption that model 1 is correct can be calculated:

$$D_{KL}\left(p_1(y)|p_2(y)\right) = \int_{-\infty}^{\infty} p_1(y)\ln\left(\frac{p_1(y)}{p_2(y)}\right) dy = \left\langle\ln\left(\frac{p_1(y)}{p_2(y)}\right)\right\rangle$$
$$= \frac{1}{2}\left\langle\ln\left(\frac{|\Sigma_2|}{|\Sigma_1|}\right) - (Y-y_1)^{\top}\Sigma_1^{-1}(Y-y_1) + (Y-y_2)^{\top}\Sigma_2^{-1}(Y-y_2)\right\rangle \qquad (25)$$

Using the properties of the multivariate normal distribution, we compute the expected values of the quadratic forms. The Kullback–Leibler divergence becomes:
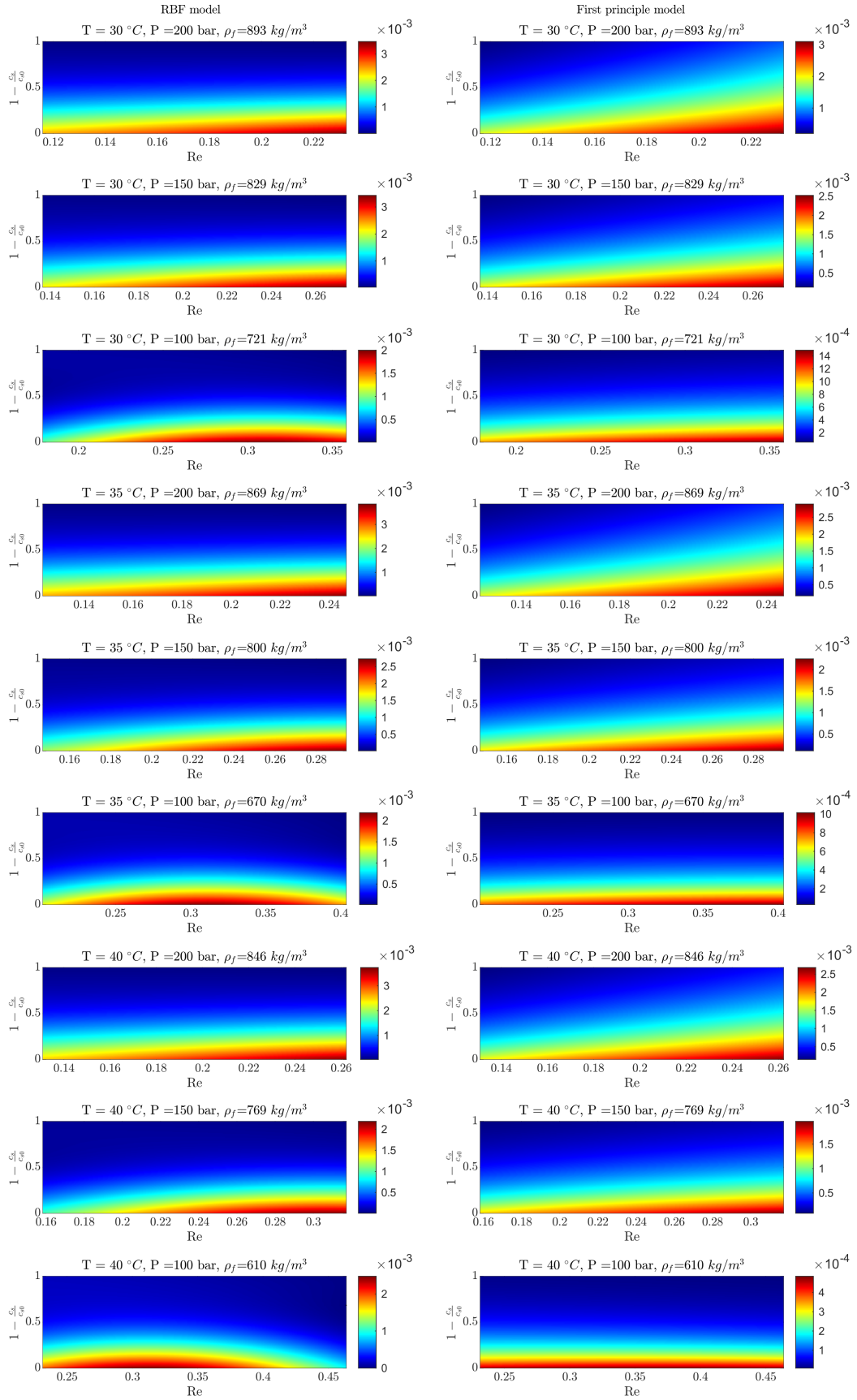
$$D_{KL}\left(p_1(y)|p_2(y)\right) = \frac{1}{2}\left[\ln\left(\frac{|\Sigma_2|}{|\Sigma_1|}\right) - n_Y + \mathrm{tr}\left(\Sigma_2^{-1}\Sigma_1\right) + (y_2-y_1)^{\top}\Sigma_2^{-1}(y_2-y_1)\right] \qquad (26)$$

Physically, the term $\ln\left(\frac{|\Sigma_2|}{|\Sigma_1|}\right)$ compares how "wide" the two models' predicted variances are overall. The $-n_Y$ arises from normalizing constants and can be seen as a base difference between two n_Y-dimensional Gaussians. The trace term $\mathrm{tr}\left(\Sigma_2^{-1}\Sigma_1\right)$ measures the mismatch between the shapes of the covariance ellipsoids (how elongated or compressed one distribution is relative to the other). The Mahalanobis distance $(y_2-y_1)^{\top}\Sigma_2^{-1}(y_2-y_1)$ measures how far apart the two mean predictions are, scaled by the covariance Σ_2.

Similarly, by interchanging the roles of 1 and 2, the analogous expression can be computed $D_{KL}\left(p_2(y)|p_1(y)\right)$ by swapping the indices. Since it is unknown which of the models is correct, both quantities are summed to represent the objective function j:

$$j = D_{KL}\left(p_1(y)|p_2(y)\right) + D_{KL}\left(p_2(y)|p_1(y)\right) = \int_{-\infty}^{\infty}\left[p_1(y)-p_2(y)\right]\ln\left(\frac{p_1(y)}{p_2(y)}\right) dy \qquad (27)$$

The experiment to be designed is the one that maximizes j. A large value of j can be obtained if $p_2(y)$ is much than $p_1(y)$, or vice versa. In either case, the outcome shows
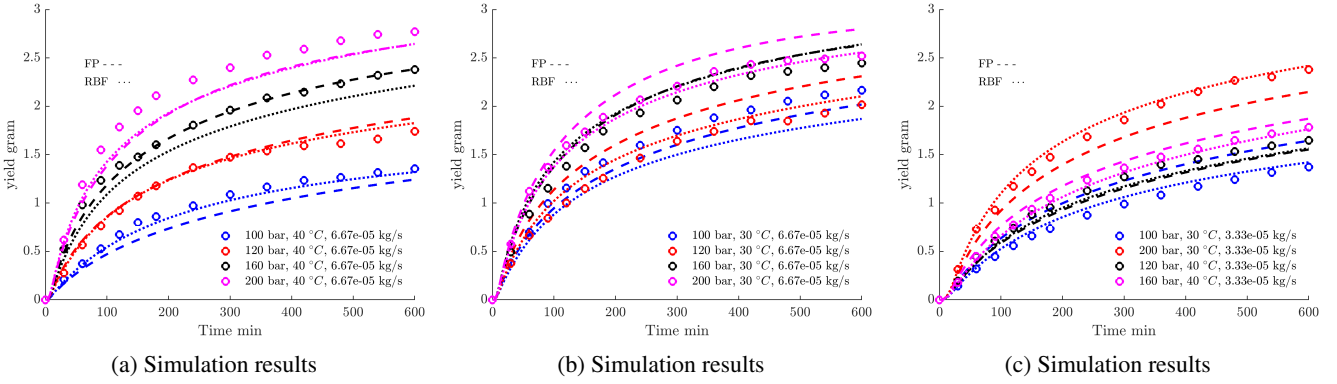
Figure 5: Comparison of the kinetic term obtained from the first principle model and the RBF model

Experiment	1	2	3	4	5	6	7	8	9	10	11	12
Mean squared error of the cumulative measurement	0.0023	0.0026	0.0252	0.0316	0.0497	0.0087	0.0205	0.0047	0.0028	0.0033	0.0060	0.0014
Mean squared error of the independent measurements	0.0003	0.0006	0.0021	0.0018	0.0012	0.0012	0.0017	0.0016	0.0001	0.0011	0.0004	0.0004
Standard deviation of error of the independent measurements	0.0182	0.0255	0.0458	0.0426	0.0274	0.0356	0.0396	0.0409	0.0094	0.0349	0.0208	0.0195

Table 2
Error between experimental data and model predictions

(a) Simulation results (b) Simulation results (c) Simulation results

Figure 6: Comparison between the First Principle model(FP), the data-driven model (RBF) and the dataset

a strong preference for one model as opposed to the other. The final form of the objective function j is given by:

$$j = -n_Y + \frac{1}{2}\left[\text{tr}\left(\Sigma_1^{-1}\Sigma_2 + \Sigma_2^{-1}\Sigma_1\right) + (y_2 - y_1)^\top\left(\Sigma_1^{-1} + \Sigma_2^{-1}\right)(y_2 - y_1)\right]$$
(28)

Σ_1 and Σ_2 as expressing the expected uncertainties or noise structures inherent in each model. The trace terms reflect how dissimilar the predicted noise covariances are, while the quadratic form indicates how far apart the two predicted mean responses lie in light of those covariances. Since one aims to design an experiment so that data sampled from the correct model would strongly disfavour the incorrect one, maximizing jj ensures that, irrespective of which model is actually correct, the measured data will most likely provide a clear discrimination between the two physical hypotheses.

4.1. Prediction of the Covariance Matrix

When using a particular model to predict an extraction yield, three distinct sources of inaccuracy typically arise: uncertainties in the estimated parameters, uncertainties in setting the experimental conditions, and measurement noise. Even if the functional form of the model itself is correct, these errors collectively produce deviations between the actual (observed) and the predicted extraction yields. In practice, there is often a small residual bias in the model's mean predictions; however, if this bias is negligible relative to the overall variability, it can be ignored in favor of a purely variance-based analysis. Under the additional assumption that these three error sources are statistically independent, the corresponding variances and covariances can be superimposed to give an approximate covariance matrix for the total prediction error.

To frame this more concretely, consider the model output $y = G(\Xi, \theta)$ as the predicted extraction yield, where Ξ represents the operating conditions (such as temperature, pressure, or solvent flow rates) and θ denotes the estimated model parameters. Let $\delta\theta$, $\delta\Xi$, and δy be the random errors associated with each of these three sources. In that case, the observed yield y_o can be written as

$$y_o = G(\Xi + \delta\Xi, \theta + \delta\theta) + \delta y$$
(29)

Here, $\delta\Xi$ captures potential deviations in how precisely the experimental conditions are implemented (for instance, if the actual temperature differs slightly from the nominal set point), $\delta\theta$ accounts for inaccuracies or uncertainties in the estimated model parameters, and δy represents measurement noise associated with the apparatus or measurement sensor.

A Taylor series expansion up to linear terms with respect to θ and Ξ results with:

$$y_o - y_p = \frac{\partial G}{\partial \Xi}\delta\Xi + \frac{\partial G}{\partial \theta}\delta\theta + \delta y$$
(30)

where $y_p = G(\Xi, \theta)$ is the model's prediction at the nominal operating conditions and estimated parameters. Physically, each partial derivative represents a sensitivity measure: it shows how the yield changes locally if the experimental conditions or the model parameters are perturbed. The product of this sensitivity with the corresponding random error, $\delta\theta$ or $\delta\Xi$, reflects how much each type of uncertainty is expected to shift the yield away from its nominal prediction.

$$\Sigma = \left\langle (y_o - y_p)(y_o - y_p)^\top \right\rangle = \frac{\partial G}{\partial \Xi}\Sigma_\Xi\left(\frac{\partial G}{\partial \Xi}\right)^\top + \frac{\partial G}{\partial \theta}\Sigma_\theta\left(\frac{\partial G}{\partial \theta}\right)^\top + \Sigma_y$$
(31)

The first term describes the additional uncertainty introduced if the experimental conditions themselves cannot be fixed exactly; it may be dropped if conditions (for example, temperature or flow rate) are perfectly controlled or have negligible variation. The second term quantifies how parameter uncertainty, arising from imperfect fitting of kinetic or equilibrium constants, propagates into the final yield predictions. The third term, reflects random noise in measuring or detecting the yield. This might stem from

instrument imprecision or environmental factors, and can be estimated either by looking at residuals from previous calibration measurements or by using specifications provided by the instrument manufacturer.

If the parameters θ are being estimated in a statistically efficient way (for instance, by a maximum-likelihood method with large-sample properties), then $\Sigma\theta$ often approaches the inverse of the Fisher information, thereby saturating the Cramér–Rao lower bound asymptotically.

4.2. Problem formulation

The optimization problem is solved for multiple cases of constant pressure: 100, 125, 150, 175 and 200 bar.

$$
\begin{aligned}
\Xi^* \quad &= \arg\min_{T^{in}, F \in \Xi} -j \\
\text{subject to} \quad & \dot{x} = G(x, t, \Theta; \Xi) \\
& t_0 = 0 \quad \text{min} \\
& t_f = 600 \text{ min} \\
& T^0 = T^{in}(t=0) \\
& P(t) \in \{100, 125, 150, 175, 200\} \text{ bar} \\
& 30°C \leq T^{in}(t) \leq 40°C \\
& 3.33 \cdot 10^{-5} \leq F(t) \leq 6.67 \cdot 10^{-5}
\end{aligned}
\tag{32}
$$

Although both models were fitted using the same dataset, they incorporate structurally different extraction kinetics, leading to distinct outputs, especially in regions not covered by the data. New experimental conditions (Ξ^*) are determined by identifying the set of controls that causes the greatest divergence between the models' outputs. The next step is to conduct the experiment and compare the results with the model predictions. The model that most accurately predicts the experimental outcome is retained for further use.

5. Results

6. Conclusions

References

[1] Gholamhossein Sodeifian and Seyed Ali Sajadian. Investigation of essential oil extraction and antioxidant activity of echinophora platyloba dc. using supercritical carbon dioxide. The Journal of Supercritical Fluids, 121:52–62, March 2017. ISSN 0896-8446. doi: 10.1016/j.supflu.2016.11.014.

[2] E. Reverchon, G. Donsi, and L.S. Osseo. Modeling of supercritical fluid extraction from herbaceous matrices. Industrial & Engineering Chemistry Research, 32(11):2721–2726, nov 1993. doi: 10.1021/ie00023a039.

[3] H. Sovova. Rate of the vegetable oil extraction with supercritical co2. modelling of extraction curves. Chemical Engineering Science, 49 (3):409–414, 1994. doi: 10.1016/0009-2509(94)87012-8.

[4] Eckhard Weidner. Impregnation via supercritical co2–what we know and what we need to know. The Journal of Supercritical Fluids, 134: 220–227, April 2018. ISSN 0896-8446. doi: 10.1016/j.supflu.2017.12.024.

[5] Noelia D. Machado, José E. Mosquera, Raquel E. Martini, María L. Goñi, and Nicolás A. Gañán. Supercritical co2-assisted impregnation/deposition of polymeric materials with pharmaceutical, nutraceutical, and biomedical applications: A review (2015–2021). The Journal of Supercritical Fluids, 191:105763, December 2022. ISSN 0896-8446. doi: 10.1016/j.supflu.2022.105763.

[6] Mostafa Fathi, Gholamhossein Sodeifian, and Seyed Ali Sajadian. Experimental study of ketoconazole impregnation into polyvinyl pyrrolidone and hydroxyl propyl methyl cellulose using supercritical carbon dioxide: Process optimization. The Journal of Supercritical Fluids, 188:105674, September 2022. ISSN 0896-8446. doi: 10.1016/j.supflu.2022.105674.

[7] Luís Padrela, Miguel A. Rodrigues, Andreia Duarte, Ana M.A. Dias, Mara E.M. Braga, and Hermínio C. de Sousa. Supercritical carbon dioxide-based technologies for the production of drug nanoparticles/nanocrystals – a comprehensive review. Advanced Drug Delivery Reviews, 131:22–78, June 2018. ISSN 0169-409X. doi: 10.1016/j.addr.2018.07.010.

[8] Paola Franco and Iolanda De Marco. Nanoparticles and nanocrystals by supercritical co2-assisted techniques for pharmaceutical applications: A review. Applied Sciences, 11(4):1476, February 2021. ISSN 2076-3417. doi: 10.3390/app11041476.

[9] Nedasadat Saadati Ardestani, Gholamhossein Sodeifian, and Seyed Ali Sajadian. Preparation of phthalocyanine green nano pigment using supercritical co2 gas antisolvent (gas): experimental and modeling. Heliyon, 6(9):e04947, September 2020. ISSN 2405-8440. doi: 10.1016/j.heliyon.2020.e04947.

[10] Gholamhossein Sodeifian, Seyed Ali Sajadian, and Reza Derakhsheshpour. Co2 utilization as a supercritical solvent and supercritical antisolvent in production of sertraline hydrochloride nanoparticles. Journal of CO2 Utilization, 55:101799, January 2022. ISSN 2212-9820. doi: 10.1016/j.jcou.2021.101799.

[11] O. Singh, Z. Khanam, N. Misraand, and M.K. Srivastava. Chamomile (matricaria chamomilla l.): An overview. Pharmacognosy Reviews, 5 (9):82, 2011. ISSN 0973-7847. doi: 10.4103/0973-7847.79103.

[12] J. Srivastava. Extraction, characterization, stability and biological activity of flavonoids isolated from chamomile flowers. Molecular and Cellular Pharmacology, 1(3):138–147, August 2009. ISSN 1938-1247. doi: 10.4255/mcpharmacol.09.18.

[13] A. Orav, A. Raal, and E. Arak. Content and composition of the essential oil ofchamomilla recutita(l.) rauschert from some european countries. Natural Product Research, 24(1):48–55, January 2010. ISSN 1478-6427. doi: 10.1080/14786410802560690.

[14] M. Goto, B.C. Roy, and T. Hirose. Shrinking-core leaching model for supercritical-fluid extraction. The Journal of Supercritical Fluids, 9 (2):128–133, jun 1996. doi: 10.1016/s0896-8446(96)90009-1.

[15] H. Sovová, J. Kučera, and J. Jež. Rate of the vegetable oil extraction with supercritical co2—ii. extraction of grape oil. Chemical Engineering Science, 49(3):415–420, 1994. ISSN 0009-2509. doi: 10.1016/0009-2509(94)87013-6.

[16] H. Sovova, R. Komers, J. Kucuera, and J. Jezu. Supercritical carbon dioxide extraction of caraway essential oil. Chemical Engineering Science, 49(15), 1994. doi: 10.1016/0009-2509(94)e0058-x.

[17] Keith D. Bartle, Anthony A. Clifford, Steven B. Hawthorne, John J. Langenfeld, David J. Miller, and Robert Robinson. A model for dynamic extraction using a supercritical fluid. The Journal of Supercritical Fluids, 3(3):143–149, September 1990. ISSN 0896-8446. doi: 10.1016/0896-8446(90)90039-o.

[18] E. Reverchon. Mathematical modeling of supercritical extraction of sage oil. AIChE Journal, 42(6):1765–1771, June 1996. ISSN 1547-5905. doi: 10.1002/aic.690420627.

[19] G. E.P. Box and W. J. Hill. Discrimination among mechanistic models. Technometrics, 9(1):57–71, February 1967. ISSN 1537-2723. doi: 10.1080/00401706.1967.10490441.

[20] Guido Buzzi-Ferraris and Pio Forzatti. A new sequential experimental design procedure for discriminating among rival models. Chemical Engineering Science, 38(2):225–232, 1983. ISSN 0009-2509. doi: 10.1016/0009-2509(83)85004-0.

[21] Bing H. Chen and Steven P. Asprey. On the design of optimally informative dynamic experiments for model discrimination in multiresponse nonlinear situations. Industrial &; Engineering Chemistry Research, 42(7):1379–1390, February 2003. ISSN 1520-5045. doi: 10.1021/ie0203025.

[22] J. D. Jr Anderson. Computational fluid dynamics the basic with applications. McGraw-Hill, 1995. ISBN 9780071132107.

[23] J. D. Jr Anderson. Fundamentals of Aerodynamics. McGraw-Hill Education, 2023. ISBN 9781264151929.

[24] N. R. Bulley, M. Fattori, A. Meisen, and L. Moyls. Supercritical fluid extraction of vegetable oil seeds. Journal of the American Oil Chemists' Society, 61(8):1362–1365, aug 1984. doi: 10.1007/bf02542243.

[25] M. Spiro and M. Kandiah. Extraction of ginger rhizome: partition constants and other equilibrium properties in organic solvents and in supercritical carbon dioxide. International Journal of Food Science & Technology, 25(5):566–575, jun 2007. doi: 10.1111/j.1365-2621.1990.tb01116.x.

[26] H. Sovova. Broken-and-intact cell model for supercritical fluid extraction: Its origin and limits. The Journal of Supercritical Fluids, 129:3–8, nov 2017. doi: 10.1016/j.supflu.2017.02.014.

[27] Oliwer Sliczniuk and Pekka Oinas. Mathematical modelling of essential oil supercritical carbon dioxide extraction from chamomile flowers. The Canadian Journal of Chemical Engineering, 2024. doi: 10.1002/cjce.25557.

[28] J. Gmehling, M. Kleiber, B. Kolbe, and J. Rarey. Chemical Thermodynamics for Process Simulation. Wiley, mar 2019. doi: 10.1002/9783527809479.

[29] Paul Antonie and Camila G. Pereira. Solubility of functional compounds in supercritical co2: Data evaluation and modelling. Journal of Food Engineering, 245:131–138, March 2019. ISSN 0260-8774. doi: 10.1016/j.jfoodeng.2018.10.012.

[30] David Mautner Himmelblau. Process analysis by statistical methods. Wiley, New York, 1970. ISBN 047139985X. [by] David M. Himmelblau., Includes bibliographical references.

[31] Yonathan Bard. Nonlinear parameter estimation. Acad. Press, New York [u.a.], 1974. ISBN 0120782502.